Dodecagonal Zinc Oxide (*d*-ZnO) Monolayer for Water Desalination and Detection of Toxic Gases

Yusuf Zuntu Abdullahi[1,2] Ahmet Tigli[3] and Fatih Ersan[1,*]

[1]*Department of Physics, Aydin Adnan Menderes University, Aydın 09010, Turkey*
[2]*Department of Physics, Faculty of Science, Kaduna State University, Kaduna State P.M.B. 2339, Nigeria*
[3]*Department of Metallurgy and Materials Engineering, Sinop University, Sinop 57000, Turkey*

Nanoporous materials have attracted great interest because of their variety of applications in nanodevices, such as gas storage, low-density magnetic storage, energy storage, supercapacitors, catalysis, membranes, etc. The most common purpose of using nanoporous materials is to make a material much lighter while preserving or improving the high structural stability of these compounds. In this work, we propose a two-dimensional dodecagonal zinc oxide (*d*-ZnO) monolayer via first-principles calculations based on density-functional theory (DFT). Our extensive analysis shows that this semiconducting porous *d*-ZnO material is mechanically, dynamically, and thermally stable and suitable for various applications, such as water membrane and gas detection at room temperature and above. We study the water permeability and Na^+ and Cl^- ions' rejection of *d*-ZnO material via conducting DFT and molecular dynamics (MD) simulations. Our simulations show that the energy barrier of the water molecule and Na^+/Cl^- ions passing through the porous *d*-ZnO structure is low and high, respectively. In addition, MD calculations show that the water permeability performance of *d*-ZnO material is high enough to use this material for water desalination applications. For further investigations, the detection of some selected gases (CO, SO, NO, CO_2, SO_2, and NO_2) are investigated on *d*-ZnO and find that NO_2, and SO_2 would preferentially be detected on the *d*-ZnO substrate due to their high adsorption energy values as compared to physisorption of CO, NO, SO, and CO_2 molecules on the *d*-ZnO surface.

I. INTRODUCTION

Two-dimensional (2D) nonmetal-contained (NMC) porous materials have been extensively studied [1,2] for basic and applied research because of their intrinsic properties [3,4] superior to other forms of 2D materials. For example, the synthesized porous graphene and its derivatives [5] have been suggested in applications, such as water purification membranes [5–12], gas separation [13,14], and energy-related fields [15,16]. The reported performance of porous graphene, particularly in gas-mixture separation applications, raised hopes that it could serve as a membrane for seawater desalination. To consolidate this objective, a stable porous graphene structure with high water permeance and selectivity towards the soluble Na^+/Cl^- ions should be further investigated. Since the performance of a membrane for gas-molecule separation and removing undesirable substances from water is related to the thickness of a monolayer and the pore electron density map [17], screening and identifying monolayers that can meet

these requirements is crucial. On this note, creating porous materials with at least two different types of atoms from the parent lattice is one way to improve selectivity in this separation process. Among them, the family of polymeric 2D carbon nitride (CN) monolayers is especially unique. This is mainly attributed to their structural diversity causing them to assume many allotropes with different sizes of porous sites. Due to their electronic structure, availability, nontoxicity, and photoredox potentials, they have been reported to hold promising prospects in clean and sustainable energy applications [18–23]. Striazine (C_6N_6) sheet is one of the most stable allotropes of CN at room temperature [24]. It is found to exhibit ideal optical absorption anisotropy for water-splitting photocatalysis [25]. In addition, it was proposed as a membrane for the purification of toxic gases and water [26–31] due to its natural pores, which have excellent H permeability and selectivity [26]. Abdullahi *et al.* revealed that single and double B-doped C_6N_6 sheets can exhibit robust ferromagnetism with half-metallicity [32]. Moreover, theoretical and experimental studies have reported [33–37] enhanced catalytic potentials of transition-metal (TM) atoms embedded in C_6N_6 (TM-C_6N_6) hybrid systems. Also, efforts have been made

*fatih.ersan@adu.edu.tr

to suggest using the TM-C_6N_6 system for gas-sensing applications [38–41].

Despite the numerous advantages of the TM-C_6N_6 hybrid systems, it is difficult to generate a uniformly dispersed TM atom without compromising the planarity of the system. On the other hand, there is always a tendency to form diatom nitrogen in the pore due to the presence of sensitive sp-hybridized N atom causing a corrugation in the system. Therefore, TM atoms can move freely on the surface and segregate to form clusters due to the nonplanarity of the system [42]. The formation of the TM complexes and their clusters on the surface would make it ineffective thereby limiting its benefits for sensing, catalysis, and related applications [43,44]. To solve this problem, it is imperative to design 2D porous materials with TM atoms from the parent 2D lattice. Until now, the theoretical pursuit of porous 2D materials has been limited to NMC systems except of the pore site created in 2D transition-metal dichalcogenides [45,46]. No theoretical work on porous TM oxides, particularly ZnO porous sheet for gas sensing and water purification has been reported. However, we are aware that ZnO has been experimentally reported for gas-sensing applications in several nanostructure forms [47–58], including porous ZnO sheet [59]. Inspired by the C_6N_6 monolayer's potential and our recently predicted 2D dodecagonal boron-nitride structure [60], it will be intriguing to theoretically search for porous ZnO with a similar B_6N_6 building block to serve as an alternative to the NMC porous system. It is believed that the porous ZnO sheet will spark a theoretical revolution in 2D metal-contained porous sheets for a variety of applications. The study would have an impact on the understanding of the porous ZnO monolayer and its application to the aforementioned properties due to the expected asymmetries in the d-ZnO structure, such as charge, pore size, and thickness, and the presence of many O active sites for chemical activity.

Based on the aforementioned experimental works on ZnO nanostructures, a porous ZnO sheet is expected to provide improved sensor performance, such as ultrahigh sensitivity at extremely low concentrations, high specificity, fast response and recovery, low energy consumption, ambient temperature operation, and good reversible resilience [61,62]. Aside from gas-sensing applications, porous ZnO sheets may also be used as a water-purification membrane. This is because of its natural antibacterial tendency to neutralize all types of water-borne bacteria and it being considered a safe substance for humans and animals [63]. According to a report, ZnO is stable under rigorous processing conditions due to its superior durability and heat resistance [64,65]. As previously mentioned, the challenge for water desalination is finding suitable porous materials with an appropriate pore size and thickness. Porous ZnO is expected to overcome these challenges as a result of its regular array of pore sites with nondangling bonds, which will provide a favorable pore electron density

size. So that weak interactions between H_2O molecules and the d-ZnO pore become advantageous for H_2O diffusion.

In this work, we predict a semiconducting dodecagonal ZnO (d-ZnO) sheet by first-principles calculations. d-ZnO exhibits excellent energetic, dynamic, mechanical, and thermal stabilities. Density-functional theory (DFT) and classical molecular dynamics (MD) calculations reveal that the d-ZnO monolayer shows excellent performance to serve as a membrane for water desalination. In further investigations, we explore the potential of d-ZnO as a substrate for the detection of some selected toxic gases and the purification of water. It has been demonstrated that the d-ZnO substrate will preferably detect toxic NO, NO_2, and SO_2 gases approaching the sheet. The fact that the majority of the studied gas molecules are soluble in water and that their detection is a crucial step in the process of purifying water. The d-ZnO is expected to favorably detect these harmful polluting gases in hydrated ionic form through the reaction of surface oxygen molecules with target hydrated molecule ions. For example, NO_2 is the main pollutant causing acid rain while SO_2 ions are one of the undesired soluble ions in seawater.

II. COMPUTATIONAL METHODS

All the calculations of the ground-state properties are performed using the Vienna *ab initio* simulation package (VASP) [66], which is based on the DFT [67] method. The exchange correlation is treated with the generalized gradient approximation (GGA) of Perdew-Burke-Ernzerhof (PBE) [68] parametrization. The Hubbard U correction [69] (PBE+U) is used to describe strongly localized d orbitals of the Zn atom. The estimated U_{eff} values for the d orbital of Zn is $U_{eff} = 9.21$ eV (see the Appendix). More information about our obtained U_{eff} values can be found in previous studies [70,71]. The projected augmented-wave (PAW) pseudopotentials method [68] is used to describe the core and valence electrons for all atoms in d-ZnO monolayers. For the dispersion correction, DFT-D2 correction of Grimme [72] is used. The irreducible Brillouin zone (BZ) in reciprocal spaces has been represented by a Monkhorst-Pack set of k-point grid meshes [73]. For optimizations and total density of state calculations we use ($6 \times 6 \times 1$) and ($12 \times 12 \times 1$) grid meshes, respectively. An energy cutoff of 500 eV is taken for plane-wave basis set expansion. A vacuum space of 15 Å along the z direction is set to eliminate interaction between the adjacent layers of d-ZnO. The criteria for convergence of the total energy and remaining force on each atom's in two iterated steps are set smaller than 10^{-5} eV and 0.01 eV/Å, respectively. The dynamic stability of d-ZnO monolayer is examined with the aid of phonon-dispersion calculations. For the phonon calculations, we employ (2×2) supercell of the d-ZnO monolayer to reduce the constraint of periodic boundary conditions. Then, we use the supercell

method of the PHONOPY code [74] to obtain phonon band structure. We perform the climbing-image nudged elastic band (CI NEB) scheme [75] to estimate the minimum energy diffusion pathways for both H_2O and Na through the pore site of the *d*-ZnO sheet. Quantum ESPRESSO (QE) code [76] is used for the CI NEB calculations. A total of seven images are used between the initial and final positions. To produce results with negligible error, we make sure that similar computational parameters, such as PAW PPs, are used for both VASP and QE computations.

To examine if the *d*-ZnO sheet will favorably capture CO, NO, SO, CO_2, NO_2, SO_2 molecules, we calculate the adsorption energy (E_{ads}) defined as

$$E_{ads} = (E_{d\text{-ZnO}} + E_{mol}) - E_{mol@d\text{-ZnO}}, \quad (1)$$

where $E_{mol@d\text{-ZnO}}$, $E_{d\text{-ZnO}}$, and E_{mol} represent the total energy of molecule on *d*-ZnO systems, the energy of *d*-ZnO sheet, and the total energy of an isolated molecule, respectively. Positive E_{ads} corresponds to either weak or strong adsorption of molecules on the *d*-ZnO surface.

Large-scale atomic and molecular massively parallel simulator (LAMMPS) [77] software is used to perform MD simulations. ReaxFF [78] molecular dynamic (MD) simulations are conducted to investigate the thermal stability and water permeability of 2D *d*-ZnO. The reaxff potential used in the simulations is the combination of the force fields published by Raymond *et al.* [79] and Fedkin *et al.* [80] for the Zn/O/H and Na/Cl/O/H interactions, respectively. Additionally, the Zn-Cl-related valence angle parameters are copied straight from that of the Cu-Cl-related angles published by Rahaman *et al.* It is noteworthy that all three force fields are from the water branch, meaning that they are transferable to each other. To integrate the Newtonian equation of motion for thermal stability 0.1-fs time step and for permeability 0.2-fs time step is used. An isothermal isobaric ensemble (NPT) is used with a Nose-Hoover thermostat and barostat with a damping constant of 0.01 and 0.1 ps for temperature and pressure, respectively. The periodic boundary condition is applied in *x*, *y*, and *z* directions. The obtained results are analyzed and visualized by using the Open Visualization Tool (OVITO) [81] software. The water molecules are created by using Visual Molecular Dynamics (VMD) software [82].

III. RESULTS AND DISCUSSION

The theoretically predicted dodecagonal porous ZnO (*d*-ZnO) sheet has hexagonal symmetry (C_{6h}^1) with the space group of *P*6/*m*, The top and side view of the supercell structure are displayed in Fig. 1(a) and the black rhombohedral line illustrates the unit cell of the *d*-ZnO sheet. This structure is similar to that of the recently predicted porous *d*-BN sheet [60]. In the unit cell, there is a total of six Zn and six O atoms and each Zn(O) atom is three

coordinated by neighboring atoms. The crystal structure is formed by two Zn_3O_3 hexagonal rings that are chemically connected in an abreast manner by a Zn—O bond. These Zn and O atoms are of two kinds according to the angle formed with their bonded atoms. Between the two Zn_3O_3 rings, the Zn—O bond forms a square structure that leaves no dangling bonds in the porous site. As depicted in Fig. 1, the side view of the optimized ZnO sheet is planar without any obvious buckling tendencies. The calculated equilibrium lattice constants ($a = b$) of the *d*-ZnO sheet are found to be 8.91 Å and 8.51 Å with respect to the PBE and PBE+*U* ($U_{eff} = 9.14$ eV, see Appendix) calculations, respectively. The estimated Zn—O bond lengths are in the range of 1.829–2.000 Å (1.747–1.894 Å with PBE+*U* calculations). These results show that the lattice constant reduces in PBE+*U* calculations. This indicates the Hubbard *U* correction produces more robust bond networks in the *d*-ZnO structure that may enhance the bond stiffness as compared to that obtained in PBE calculations. Consequently, it is expected that the inclusion of the Hubbard *U* parameter will affect the electronic feature of the *d*-ZnO sheet.

To determine the chemical bonding nature in the ZnO structure, we plot the electron localization functions (ELFs). The ELF takes the values in the range of 0 to $1e^-/\text{Å}^3$ [see Fig. 1(b)]. As displayed in Fig. 1, it is clear that the ionic bonding in the *d*-ZnO structure dominates due to the concentration of charge density around the O atom, which is absent around the Zn atom. The charge localization around the O atom validates its dominant electronegativity over the Zn atom. Bader charge analysis [83] shows that the charge transfers of around $1.19e^-$ occur from the Zn atom into the O atom.

To assess the stability of the structure, we first consider the energetical stability of the *d*-ZnO sheet. For this reason, we evaluate both the cohesive energy (E_{coh}) and formation energy (E_{form}) per atom. The E_{coh} is obtained using the following equation:

$$E_{coh} = (6E_{Zn} + 6E_O - E_{d\text{-ZnO}})/12, \quad (2)$$

where E_{Zn} and E_O denote the spin-polarized total energy of an isolated Zn and O atom, respectively. E_{ZnO} represents the total energy of the *d*-ZnO sheet. The estimated E_{coh} for the *d*-ZnO, sheet is 3.29 eV/atom. The E_{coh} value is comparable to some reported stable 2D sheets, such as Mn_2C (3.35 eV) [84] and silicene (3.71 eV) [85] sheets. The E_{form} is then estimated as

$$E_{form} = (E_{d\text{-ZnO}} - 6\mu_{Zn} - 6\mu_O)/12, \quad (3)$$

where μ_{Zn} and μ_O denote the chemical potentials of Zn and O atoms. The μ_{Zn} and μ_O are estimated from the per atom energy of bulk Zn structures with space group *P*63/*mmc* and from the O_2 molecule, respectively. The calculated
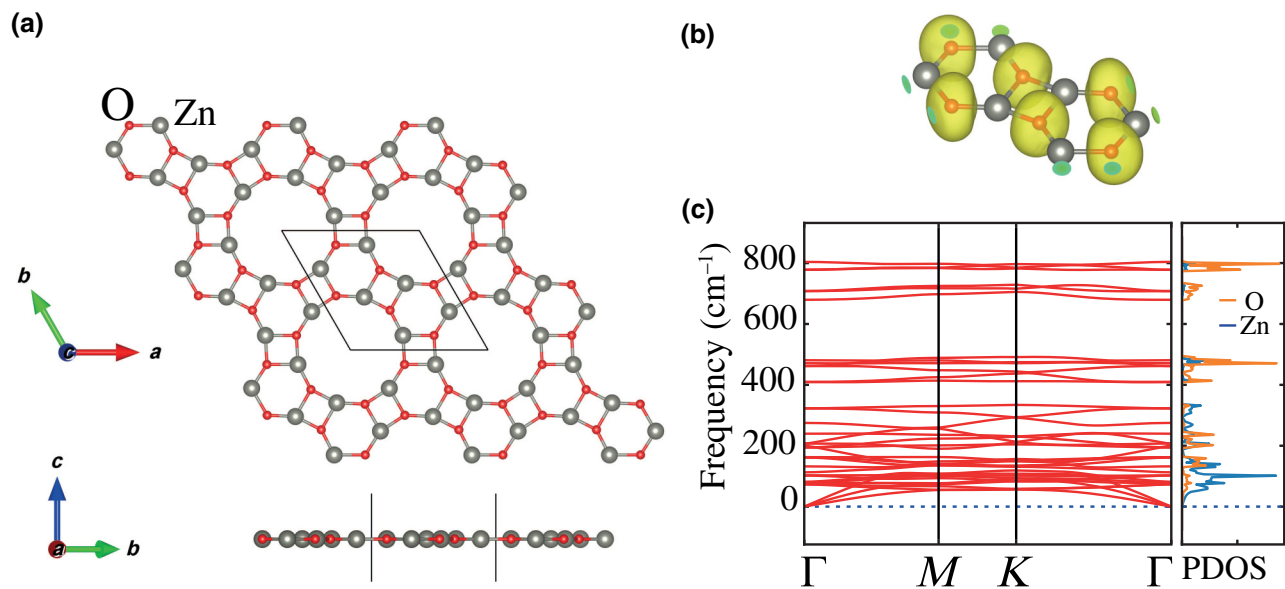
FIG. 1. (a) Top and side view of the supercell structure of the d-ZnO sheet, the solid lines show the unit cell of the d-ZnO. Red balls illustrate the O atoms while the gray balls depict the Zn atoms. (b) Electron localization functions (ELFs) for the d-ZnO sheet. The ELF isosurface value is $0.28e^-/\text{Å}^3$. (c) Phonon dispersion curve and the corresponding atom-projected phonon density of states for the d-ZnO sheet.

E_{form} (-1.12 eV/atom) is negative showing that the d-ZnO sheet is thermodynamically stable and holds promise for the experimental synthesis. All E_{coh} and E_{form} results verify that the d-ZnO sheet is energetically feasible.

As a further check on the stability of the d-ZnO sheet we investigate the mechanical properties and we compute the in-plane stiffness (Y) and Poisson's ratio (ν) of the d-ZnO sheet using the strain-energy approach [86,87]. The calculated Y and ν along the x or y strain directions are 46.89 N/m and 0.55, respectively. The positive Y and ν values are isotropic, which means that they satisfy the minimum Born criteria for elastic stability of hexagonal 2D materials [88]. The estimated Y and ν values also illustrate the good mechanical stability of the d-ZnO sheet. In comparison, the Y value is consistent with those of SiC (48 N/m) and GaAs (48 N/m) [87].

The phonon-dispersion calculation is carried out to examine the dynamical stability of the d-ZnO sheet. As clearly demonstrated in Fig. 1(c), the spectrum of phonons is free of imaginary modes throughout the first Brillouin zone. The absence of imaginary modes ascertains the dynamical stability of the d-ZnO sheet. As illustrated in Fig. 1, the lowest three phonon-dispersion curves correspond to three acoustic branches, comprising the in-plane longitudinal acoustic (LA) branches, the transverse acoustic (TA) branches, and the out-of-plane transverse acoustic (ZA) branches. It can also be noted that the LA and TA branches show linear dispersion while the ZA branch has a quadratic form in the vicinity of the Γ point. The lattice thermal conductivity and the group velocity are driven

by these acoustic phonon modes. The highest frequency of the ZnO sheet reaches up to 800 cm^{-1}, comparable to most of the well-known 2D materials. As illustrated in the PDOS plot [see Fig. 1(c)], the atomic vibration contribution in the porous d-ZnO structure varies according to the atom weights, i.e., the highest vibration frequency originates from the lighter O atom, which confirms that frequency is proportional to the square root of atomic mass. So, we can say that the porous d-ZnO sheet is robust material owing to its high optical vibration modes. It should be noted that all the stability calculations are done using PBE calculations.

To investigate the thermal stability of the d-ZnO sheet, we use LAMMPS software. For these calculations, two different sizes of d-ZnO nanosheets (8×6.2 and 5.3×4.6 nm^2 with 15 nm vacuum length) are created [see Fig. 2(a)] and heated up to 1400 with 100 K increments in order to investigate the suitability of the selected potentials for the dodecagonal zinc oxide structure. This heating simulation for a relatively short simulation time shows that the reaxff potential used is suitable for further calculations to investigate the water permeability property of d-ZnO (see Appendix for details). After these simulations, the thermal stability of d-ZnO nanosheets is investigated using these reaxff potentials for MD simulations at 300 K (for 2 ns) and at 400 K for 10 ns. As can be seen from Fig. 2(b), the d-ZnO monolayer structure retained the structural integrity and there are only thermal fluctuations during 10 ns in a 400-K simulation, suggesting that the d-ZnO sheet is thermally stable.
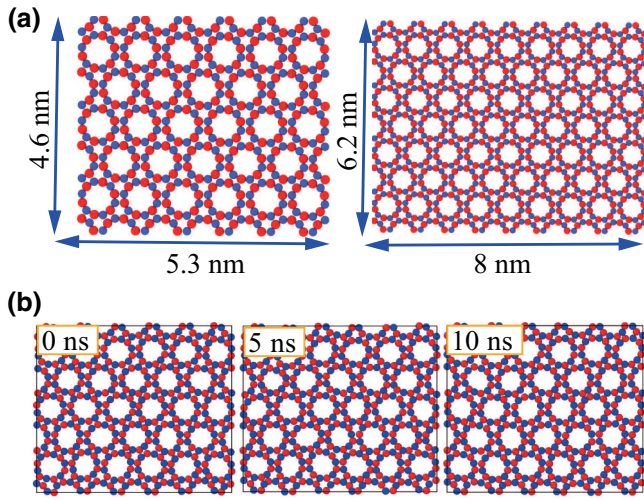
FIG. 2.   Snapshots of the first frame of heating simulations of *d*-ZnO nanosheets (a) 4.6 × 5.3 nm and 6.2 × 8.0 nm sized and (b) top views of the snapshots of the atomic configurations of the *d*-ZnO nanosheet taken from MD simulations at 400 K for of 0, 5, and 10 ns. Red and blue balls represent Zn and O atoms, respectively.
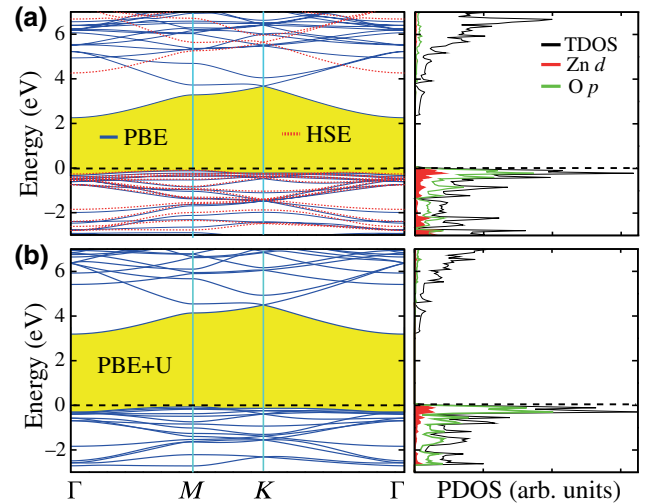

FIG. 3.   The electronic band structure and the corresponding atom orbital projected density of state of the *d*-ZnO sheet for (a) PBE, HSE and (b) Hubbard *U* functionals. The Fermi energy level is set to zero eV. The band gap is colored with yellow for PBE and PBE+*U* calculations.

Considering the good energetic, dynamic, and thermal stabilities, it would be beneficial to discuss the possible method for the experimental synthesis of the *d*-ZnO monolayer. As is widely known, van der Waals (vdW) epitaxial growth has been the most feasible way to grow a monolayer crystal on a substrate [89,90]. This method is equally valid for heteroepitaxy with a reasonable lattice mismatch and a substrate surface free of dangling bonds [91,92]. To achieve a good lattice match for *d*-ZnO epitaxial growth, the experimentally synthesized C_2N [92], AlSb [93], AlN [93], and InSb [94] monolayers can be proposed as substrates, i.e., a unit cell of *d*-ZnO ($a = 8.9$ Å) and a unit cell of C_2N ($a = 8.33$ Å), or a supercell of $2 \times 2 \times 1$ AlSb ($a = 8.66$ Å), $2 \times 2 \times 1$ InSb (9.14 Å), and $3 \times 3 \times 1$ AlN (9.27 Å) monolayers should be used to form *d*-ZnO/C_2N, *d*-ZnO/XSb, and *d*-ZnO/AlN heterostructures with a minimal lattice mismatch of 6.5%, 2.7%, 2.6%, and 4.0%, respectively. Thus, the *d*-ZnO could be produced by the chemical vapor deposition (CVD) method from these heterostructures as previously reported for related vdW heteroepitaxy [89–92].

Having established the stability of the *d*-ZnO sheet, the electronic property is then examined. Because the *d*-ZnO sheet involves strongly correlated atoms, the PBE+*U* calculations are considered. The PBE and PBE+*U* band structures and their corresponding projected density of states (PDOS) of the *d*-ZnO sheet are shown in Fig. 3. It should be noted that even though we optimize the ZnO sheet with spin-polarized calculations, we obtain a nonmagnetic semiconducting structure with indirect band gaps of 2.38 eV (PBE) and 3.26 eV (PBE+*U*). The semiconducting

property is further validated by HSE06 hybrid functional calculation [see Fig. 3(a)] and find that the obtained band-gap value (4.36 eV) is well above the PBE+*U* (3.26 eV) results. As displayed in the plot, the increase in band gap for both PBE+*U* and HSE calculations is due to the shift of conduction-band minimum (CBM) to the region of higher energy. The valence-band maximum (VBM) is situated at the *M* high symmetry point while the CBM is at the Γ point in the band structure. The dominant orbital contribution to the VBM comes from the *p* and *d* orbitals of O and Zn atoms while these orbitals become delocalized at the CBM. The presence of nearly flat bands at the VBM is a useful feature that could lead to large effective masses of holes due to the wide radius of curvature. We expect large correlation effects [95–97] from the large localization of holes. This may result in unusual phenomena like the fractional quantum Hall effect [98,99] and room-temperature ferromagnetism and antiferromagnetism [100–103].

A. The permeability of the *d*-ZnO sheet for water molecule

First, we look at the geometrical features of the *d*-ZnO pore environment. As displayed in Fig. 1, both Zn and O atoms contribute equally to the pore site with no dangling bonds. The lowest optimized distance between the two symmetrically opposite atoms in the pore is 6.99 Å (the diameter of the pore). The pore size of *d*-ZnO is sufficiently adequate to function as a membrane for salt rejection rate and water flux permeation. This is because the obtained pore diameter value (6.99 Å) is smaller than the diameter of the Na^+ ion (7.5 Å) but larger than the size of a water
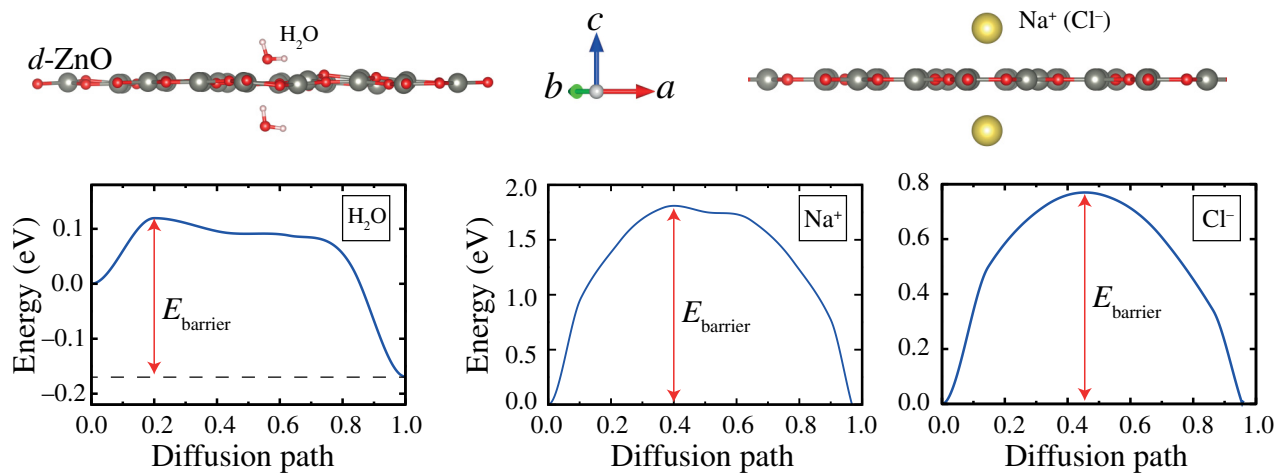
FIG. 4. The side view of the atomic configurations for the d-ZnO sheet with the illustration of the initial and final images of the NEB calculations. The calculated minimum energy profile for the permeability of the d-ZnO sheet for the H_2O molecule, Na^+, and Cl^- ions.

molecule (4.0 Å) [104]. The desalination process involving Cl^- ion (6.5 Å) can be improved by applying mechanical strain, as was reported for the C_2N monolayer, which has a comparatively smaller pore diameter for water flux permeation. It was found that the water flux permeation into the C_2N pores performed better at 12% biaxial tensile strain [105]. However, we suppose that our predicted single-layer d-ZnO can be a good membrane for water desalination with its suitable pore size.

According to the ELF plot [see Fig. 1(b)], the O atoms would supposedly make the pore environment highly electron rich due to dominant Zn—O ionic bonding. Consequently, this pore site may favorably trap a positively charged cationic atom (e.g., Na^+ ion) and repels negatively charged ions (e.g., Cl^- ion) as compared with a polar molecule (e.g., H_2O). Another consideration in deciding whether the ZnO sheet can absorb these atoms without considerable structural reconstruction is the magnitude of the ionic radii of Na (0.132 nm), Cl (0.181), and O (0.128 nm) atoms. The ionic radius of Na^+ and Cl^- is larger than that of the O atom. This suggests that the Na^+ and Cl^- ions probably could not pass through from the center of the pore site while the water molecule can pass easily. To test our hypothesis, we first investigate the adsorption mechanism of the H_2O molecule and the adatoms Na^+/Cl^- on the (2×2)-ZnO supercell. Initially, the H_2O molecule and Na^+ ion are attached at a specific height ($h = 2$ Å) above the center of the ZnO pore site. All atoms in the ZnO with adsorbed H_2O ($H_2O@ZnO$), Na (Na@ZnO), and Cl (Cl@ZnO) systems are fully relaxed and free of any geometry constraints. At the end of optimization, both the Na@ZnO and the Cl@ZnO systems remain planar with no noticeable tendency for corrugation in the systems. Only a few Zn/O atoms move in and out of the ZnO plane by 0.07/0.2 Å due to the strain that gets generated during the Na embedment. It is also noted that the Na^+ ions are embedded in the center of the pore site and forms a perfect symmetric bond with the surrounding atoms while the Cl^- forms a bond with one of the edge Zn atoms. The estimated distance between the Na and nearest Zn/O atoms along the edge of the pore is in the range of 3.54–3.56 Å and that of Cl^- with the bonded Zn atom is 2.36 Å. The calculated adsorption energies are 0.697 and 1.41 eV for Na and Cl adatoms, respectively. According to Bader's charge analysis, Na^+ transfers $0.71e^-$ to the ZnO sheet while Cl^- gains about $0.56e^-$ from the d-ZnO sheet. The charge transfer will influence the permeability of both Na^+ and Cl^- ions, making them difficult to pass through the pore in addition to the steric repulsion. In contrast to both Na^+ and Cl^- ions, H_2O gets adsorbed at a given height on the ZnO surface. Non-noticeable structural reconstruction can be seen in the $H_2O@ZnO$ system. Only a few Zn/O atoms move in and out of the ZnO plane by the same amount as in the case of the Na@ZnO system. Due to a difference in the ionic interaction, the lower O atom of the adsorbed H_2O forms an asymmetric bonds' network with those in the d-ZnO sheet. As a result, the estimated h between the lower O atom of H_2O and those Zn/O atoms along the edge of the pore is in the range of 3.50–3.92 Å. These h values indicate a weaker vdW interaction than that obtained in the Na@ZnO and Cl@ZnO systems. In addition, the calculated adsorption energy is 0.144 eV for the H_2O molecule, which is equally lower than those for Na@ZnO and Cl@ZnO systems. Unlike in the case of Na^+, the adsorbed H_2O molecule acquires $0.04e$ from the ZnO sheet. In summary, the optimized structural properties of $H_2O@ZnO$ and Na@ZnO support our previous hypothesis that Na^+ and Cl^- ions would not be favorable to passing through the porous site while the H_2O molecule can be.
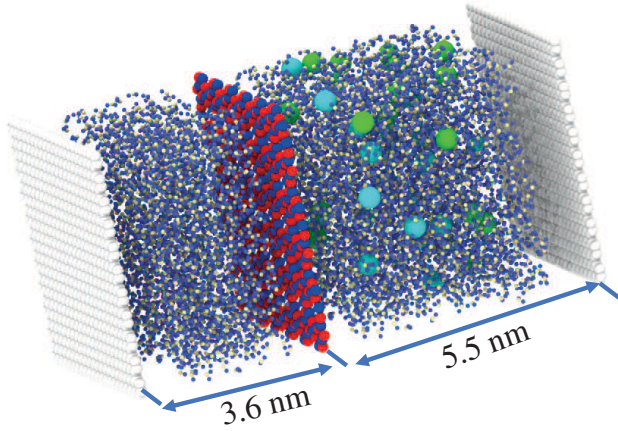
FIG. 5. The perspective view of the water-permeability simulation box. Red, blue, gray, white, aqua blue, and green balls represent Zn, O, H, and C atoms and Na$^+$, Cl$^-$ ions, respectively.

We then estimate the minimum diffusion energy barrier ($E_{barrier}$) to examine the permeability of the ZnO sheet for H$_2$O molecules and Na$^+$ ion. To seek the $E_{barrier}$ we use the CI NEB method [75]. For these calculations, we choose initial and final images, which are the top and the bottom of the center of the porous site of the *d*-ZnO structure both of them are fully optimized, and then seven intermediate images with equal intervals are linearly chosen between them. At the end of calculations, energy versus diffusion path curves plotted as illustrated in Fig. 4. The calculated $E_{barrier}$ for the H$_2$O molecule is 0.29 eV while those for the Na$^+$ ion and the Cl$^-$ ion are 1.81 and 0.77 eV, respectively. The larger $E_{barrier}$ for Na@ZnO/Cl@ZnO systems reveal a strong interaction between Na$^+$ ion and Cl$^-$ ions and Zn/O atoms along the edge of the pore. These values may show that when H$_2$O passes through the pore, the Zn/O atoms near the pore's edge will not hinder the diffusion than that observed for the Na$^+$ ion and Cl$^-$ ion cases due to weak interaction. We should note that Na$^+$ and Cl$^-$ ions will be surrounded by a spherical shell of water molecules named as hydrated ions in the salty water and this will also increase their radius. So, we can conclude that the calculated $E_{barrier}$ for the hydrated Na$^+$ and Cl$^-$ ions will be larger than the values we obtain.

We then employ the Arrhenius equation [106] to estimate the H$_2$O selectivity of the *d*-ZnO monolayer relative to the Na$^+$ and Cl$^-$ ions. The selectivity as a ratio of their diffusion rates is expressed.

$$D_{H_2O}/\text{ions} = \frac{r_{H_2O}}{r_{\text{ions}}} = \frac{C_{H_2O}\exp(-E_{H_2O}/k_B T)}{C_{\text{ions}}\exp(-E_{\text{ions}}/k_B T)}. \quad (4)$$

Here r and C represent the diffusion rate and the diffusion prefactor of H$_2$O and ions. k_B and T represent the Boltzmann constant and temperature. $E_{H_2O}(E_{\text{ions}})$ is the diffusion energy barrier (at zero temperature). Assuming the C of H$_2$O and Na$^+$/Cl$^-$ ions are constant [107]. The selectivities of H$_2$O/Na$^+$ and H$_2$O/Cl$^-$ at room temperature ($T = 300$ K) are 1.8×10^8 and 1.7×10^{65}, respectively. It is noted that the *d*-ZnO monolayer selectivity for H$_2$O molecules relative to Na$^+$/Cl$^-$ ions is high. The high selectivities indicate that H$_2$O can be effectively separated from salty seawater. As a case of comparison, nanoporous MoS$_2$ with a pore size of 6.0 Å, which is comparable to that of the *d*-ZnO monolayer, is reported to be selective for a H$_2$/CO$_2$ gas mixture [108]. The reported selectivity for H$_2$/CO$_2$ is 1.4×10^8, which is far below that for H$_2$O/Na$^+$ (1.7×10^{65}) but comparable to that of H$_2$O/Cl$^-$ (1.8×10^8). We can therefore conclude that ZnO is a qualified salty-water-purification membrane according to the CI NEB results.

In addition to the DFT calculations, the water permeability of *d*-ZnO is investigated by MD calculations with using uniaxial compression of water molecules between rigid graphene and *d*-ZnO nanosheets. A sandwichlike graphene/water/*d*-ZnO/water/graphene composite is modeled for water-permeability simulations, where the interlayer distances between graphene and *d*-ZnO nanosheets are 5.4 and 3.6 nm. An orthogonal simulation box with the dimensions of $5.3 \times 4.6 \times 15$ nm^3 is created longer at z directions to allow water molecules to pass through nanosheets (Fig. 5). The *d*-ZnO nanosheet is fixed while rigid graphene nanosheets are movable in z directions. Therefore, these graphene nanosheets are used to create external pressure to force water molecules to the *d*-ZnO nanosheet. The water molecules are created by using VMD software. 20 Na$^+$ and 20 Cl$^-$ atoms are randomly placed into the right part (between the first graphene sheets and *d*-ZnO) of the simulation box. At the left part of the simulation box, only pure water molecules are placed.

The water-permeability simulations are conducted at three stages, which are heating, holding, and compression. In the heating investigation, water molecules, *d*-ZnO, and graphene sheets are heated from 0 to 300 K during 10 ps using a *NVT* ensemble. During this heating simulation, the water molecules, which are placed at both parts of the simulation box slide through to the *d*-ZnO nanosheet [see Fig. 6(a) for 0-, 2-, 4-ps snapshots]. At the end of the heating simulations, we trace the number of water molecules that passed from the pure water side to the saline water side. To observe the water flux through the *d*-ZnO nanosheet, we keep the simulation box at 300 K for an additional 10 ps by *NPT* ensemble. In these holding simulations, we observe that the water molecules wetted the *d*-ZnO structure and the number of water molecules penetrating from the clean side to the saline side increased a little more without additional uniaxial compression [Fig. 6(a), 10- and 20-ps snapshots].
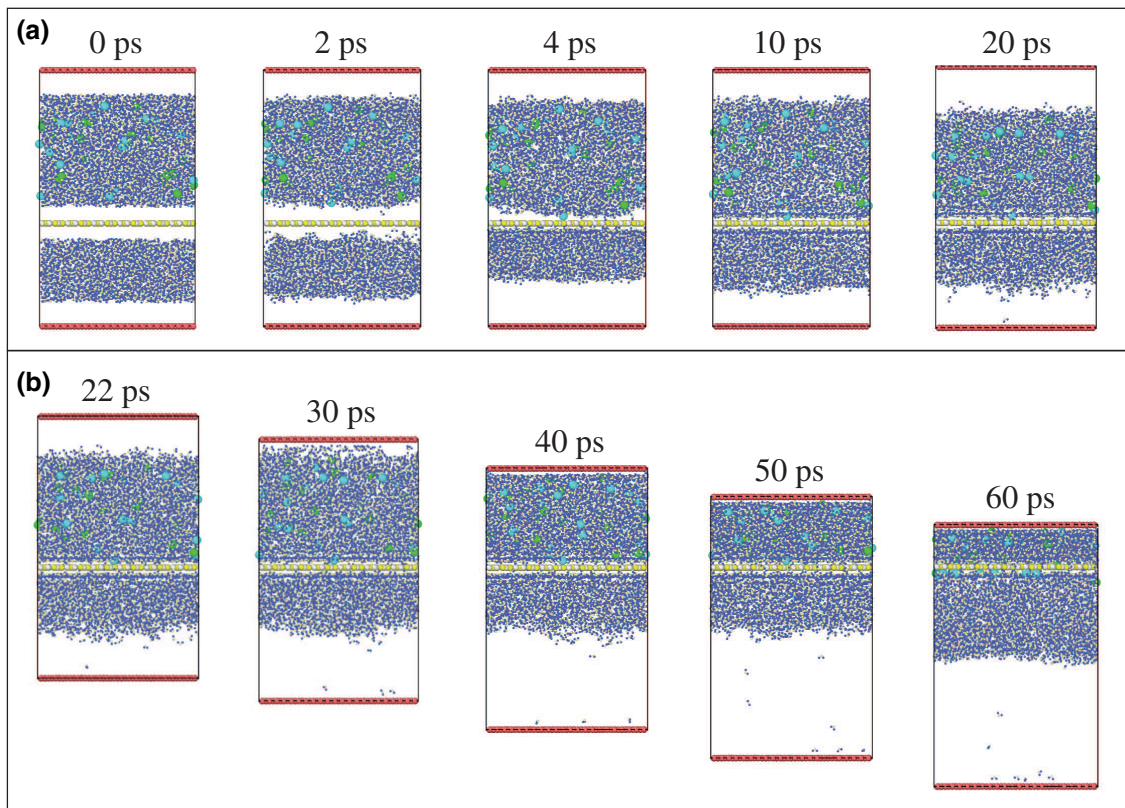
FIG. 6.   (a) The simulation snapshots of the *d*-ZnO structure at 300 K for heating and holding simulations for the initial atomic configurations and for 2, 4, 10, and 20 ps. (b) The simulation snapshots of *d*-ZnO structure at 300 K for compression simulations and atomic configurations for 22, 30, 40, 50, and 60 ps. Red, yellow, gray, blue, aqua blue, and green balls represent C, Zn, O, and H atoms and Na^+ and Cl^- ions, respectively.

However, we should note that this water flux remains again in the range of trace amount and the Na^+ and Cl^- ions did not go through the *d*-ZnO pores during the heating and the holding simulations. So, we can attribute this situation to the regular osmotic process to equalize the solute concentrations on both sides. We observe that the volume of the simulation box expanded by 6%, so the pressure remains constant in this simulation.

After the heating simulations, the graphene nanosheet starts moving at a constant speed of 0.0001 Å/fs to exert pressure on the saltwater box [see Fig. 6(b)]. We perform the compression simulation from 20 to 60 ps (with 230 000 steps). We allow the graphene sheet to move 4.6 nm in the *z* direction during this simulation, and there is a 0.9-nm distance between the graphene and *d*-ZnO nanosheets for the final simulation frame (60 ps), implying that there is an ignorable interaction between these nanosheets. With the movement of the graphene nanosheet, the passing of water molecules (from the saline water side to the pure water side) through the *d*-ZnO nanosheet starts to increase. As can be seen from Fig. 6(b), Na^+ and Cl^- ions cannot pass through the *d*-ZnO pores for 50 ps. However, there

are some Na^+ and Cl^- ions that can be seen for 60 ps due to the increased applied pressure.

To count the instantaneous number of atoms during the compression simulations, the simulation box is divided into 200 bins in the *z* direction from -100 to 50 nm (these positions are chosen to observe the motion of graphene nanosheet). Figure 7 represents the number of atoms at the *z* direction for 0, 10, 20, 30, 40, 50, 60, and 66 ps. In this figure, carbon atoms for graphene nanosheets are placed at -44 and 44 Å, respectively, and illustrated with an orange solid line while the atoms (Zn and O) for *d*-ZnO are placed at -9 Å and illustrated with a red solid line. As can be seen from these plots, a graphene nanosheet sweeps and compresses saltwater molecules until the simulation is complete. At 10 ps, the atomic density increases up to 400 atoms inside the adjacent bin (-11 and -6 in the *z* direction) of the *d*-ZnO. With the movement of the graphene piston, the water molecule density increases up to 600 atoms close to the ZnO nanosheet, see Fig. 7 (50 and 60 ps). On the other hand, the atomic density on the surface of the graphene piston increases up to 800. At 66 ps, the majority of the water molecules pass through pure
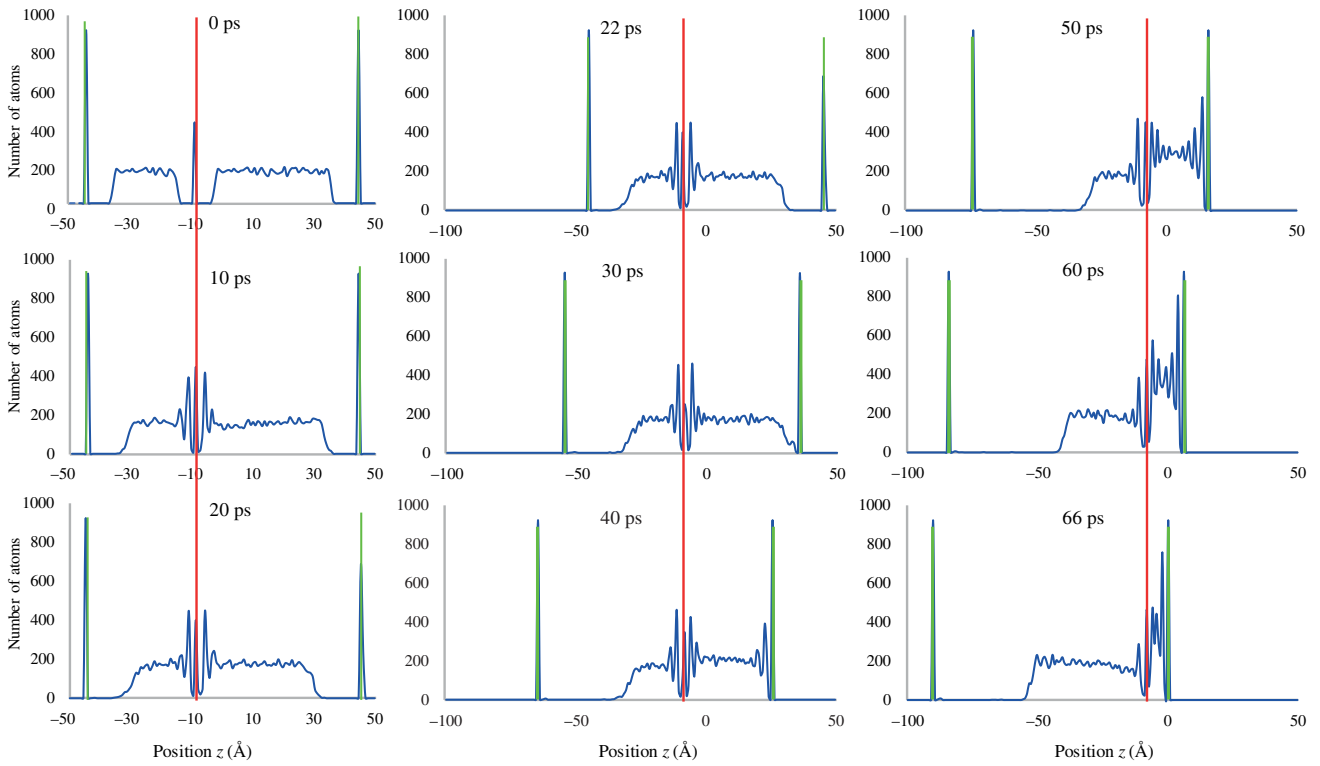
FIG. 7. The number of atoms at z positions in the water-permeability simulation box for 0, 10, 20, 22, 30, 40, 50, 60, and 66 ps. Red, green, and blue solid lines represent the *d*-ZnO, graphene, and water molecules, respectively.

water sides. During this time, some of the Na^+ and Cl^- ions also pass due to the high z-direction compression of water molecules.

Figure 8(a) illustrates the internal pressure during the simulation time and Fig. 8(b) shows the number of passed and left water molecules, Na^+ and Cl^- ions through the pore of the *d*-ZnO nanosheets at 300 K. The internal pressure in the simulation box is almost constant and nearly 0 GPa until 40 ps. With the increase in the compression rate, the internal pressure is also increased up to 1.4 GPa at 55 ps due to the increase in interatomic repulsive force between the molecules-molecules, molecules-ions, and molecules (ions)-*d*-ZnO membrane. Increasing the applied pressure results in the passing of some Na^+ and Cl^- through the pore of the *d*-ZnO nanosheet so, the pressure slightly decreases after the passing of Na^+ and Cl^- ions. This fluctuation in the pressure might be based on the blocking of the natural pores of *d*-ZnO by Na^+ and Cl^- ions. However, Fig. 9(b) shows that *d*-ZnO might be used for the desalination process. The number of water atoms passing the *d*-ZnO nanosheet is limited for both passing from the saline water part to the pure part or from the pure part to the saline water until 50 ps, while increasing the applied pressure causes the increase of the passing rate after 50 ps. The water-permeation rate at 65 ps is 69%, which means 2000 water molecules pass through the *d*-ZnO from the 2900 water molecules, which are in the saline water part. This

MD simulation reveals that the *d*-ZnO membrane might be a suitable reverse osmosis membrane material for water desalination.

B. Adsorption of (CO, NO, SO, CO₂, NO₂, SO₂) molecules on the ZnO sheet

We first search for the energetically favorable high-symmetric adsorption sites for the six (CO, NO, SO, CO_2, NO_2, SO_2) molecules on the *d*-ZnO sheet. Seven initial adsorption sites are identified on the (2×2) supercell of the ZnO sheet. The adsorption sites for these gas molecules are at the top of the Zn (T_{Zn}), O (T_O), hollow1 (T_{H1}), hollow2 (T_{H2}), bridge1 (T_{bri1}), bridge2 (T_{bri2}), and square (T_S) (see Fig. 9). All atoms in the *d*-ZnO sheet with adsorbed molecule (mol@ZnO) systems are allowed to move freely without any structural constraint during optimization. The *d*-ZnO sheet remains planar with no sign of buckling in the structure after the molecules are adsorbed except for the SO₂@ZnO case. The SO₂@ZnO shows tendencies for reconstruction on the surface. The stable adsorption sites for the NO/SO on ZnO (NO/SO@ZnO) systems and CO_2 on *d*-ZnO (CO_2@ZnO) system are at the top of the O atom and bridge, respectively, whereas the remaining (CO, NO_2, SO_2) molecules energetically preferred the hollow site. The estimated adsorption height (h) between the lowest atom of the adsorbed molecules and the ZnO sheet is 3.92 Å, 2.57 Å, 3.03 Å, 3.25 Å, 3.82 Å, 1.52 Åfor CO, NO, SO,
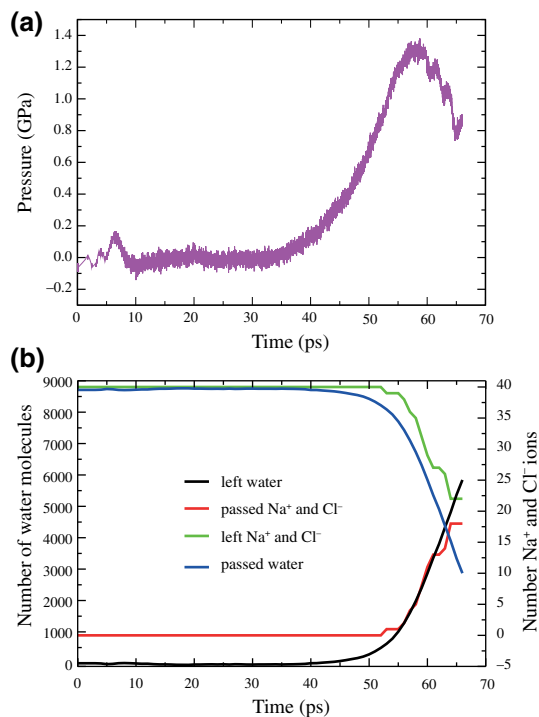
FIG. 8.   (a) The pressure in the simulation box versus time and (b) the number of passed and left water molecules, Na^+ and Cl^- ions versus time.

CO_2, NO_2, SO_2, respectively. It is clear that the shortest h value occurs for SO_2 (1.52 Å), which suggests a strong binding tendency upon approaching the ZnO sheet. This further confirms the buckling tendencies of the $SO_2@ZnO$ system.
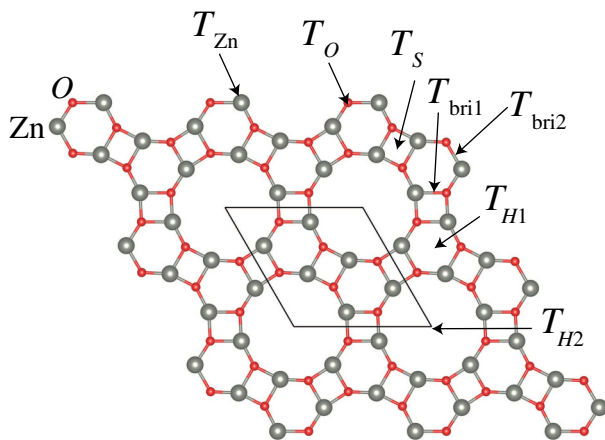

FIG. 9.   The adsorption sites for molecules are illustrated on the figure, which are on top of Zn (T_{Zn} , O (T_O), hollow1 (T_{H1}), hollow2 (T_{H2}), bridge1 (T_{bri1}), bridge2 (T_{bri2}), and square (T_S).

The calculated E_{ads} values are 0.01, 0.12, 0.08, 0.05, 1.37, 0.72 eV for CO, NO, SO, CO_2, NO_2, SO_2, respectively. For strong chemisorption, the E_{ads} value should be larger than 1 eV [109]. Our calculated E_{ads} values reveal that strong chemisorption is favorable for NO_2, while others are either chemisorbed (SO_2), weakly chemisorbed (NO), or strongly physisorbed (SO, CO, and CO_2). The optimized structures are illustrated in Fig. 10. The weak-adsorption energies for CO, NO, SO, and CO_2 imply that NO_2, and SO_2 would preferentially be detected on the d-ZnO substrate as compared to CO, NO, SO, and CO_2 molecules when these gases are simultaneously released at the constant pressure on the d-ZnO surface. Also the differences in E_{ads} values can be understood in terms of the difference in electronegativity of the atoms in the mol@ZnO systems. So we calculate the electron transfer between the adsorbed molecules and the ZnO sheet. Bader charge analysis indicates that all adsorbed molecules transfer electrons to the ZnO sheet. The estimated values are 0.013, 0.085, 0.034, 0.021, 0.060, 0.157 e for CO, NO, SO, CO_2, NO_2, SO_2, respectively. It is clearly evident that E_{ads} values correspond well with the electron transfer between the adsorbed molecules and the d-ZnO sheet.

We further examine the effects of temperature on mol@ZnO systems. The calculations in this part are carried out using *ab initio* molecular dynamics (AIMD) simulations with a time step of 3.0 fs at 300 K. The temperature is controlled using the Nose Hoover thermostat [110]. Starting from the relaxed mol@ZnO systems, all atoms in the system are allowed to move freely without any geometry restrictions during the MD calculations. As displayed in Fig. 11,CO, CO_2, NO, and NO_2 are trapped through weak physisorption at 300 K. Our PBE results at 0 K are confirmed by the weak physisorption of NO, CO, and CO_2 molecules on the ZnO surface. However, we find a clear contradiction for the $NO_2@ZnO$ case, where NO_2 is strongly chemisorbed for PBE calculations at 0 K. It can be inferred that at 300 K, the d-ZnO surface appears to be unsuitable for CO, CO_2, NO, and NO_2 gas sensors. Interestingly, the SO molecule, which is weakly physisorbed at 0 K, decomposes into S and O at 300 K on the d-ZnO sheet. To confirm this calculation, we also run MD calculations at 300-K temperature for SO molecules in the cube simulation cell, and no decomposition is observed for SO molecules. So, we believe that the reactivity processes that occur during the SO decomposition on the d-ZnO surface at 300 K should be investigated in detail in a separate study. It is also worth noting that SO_2 has a comparable chemical adsorption pattern and energy on the ZnO surface. Because SO_2 strongly interacts on the d-ZnO surface with relatively low E_{ads} value, we anticipate SO_2 decomposition with low activation energy.

The bare d-ZnO sheet is a nonmagnetic semiconductor, but upon adsorption of the NO, SO, NO_2 molecules
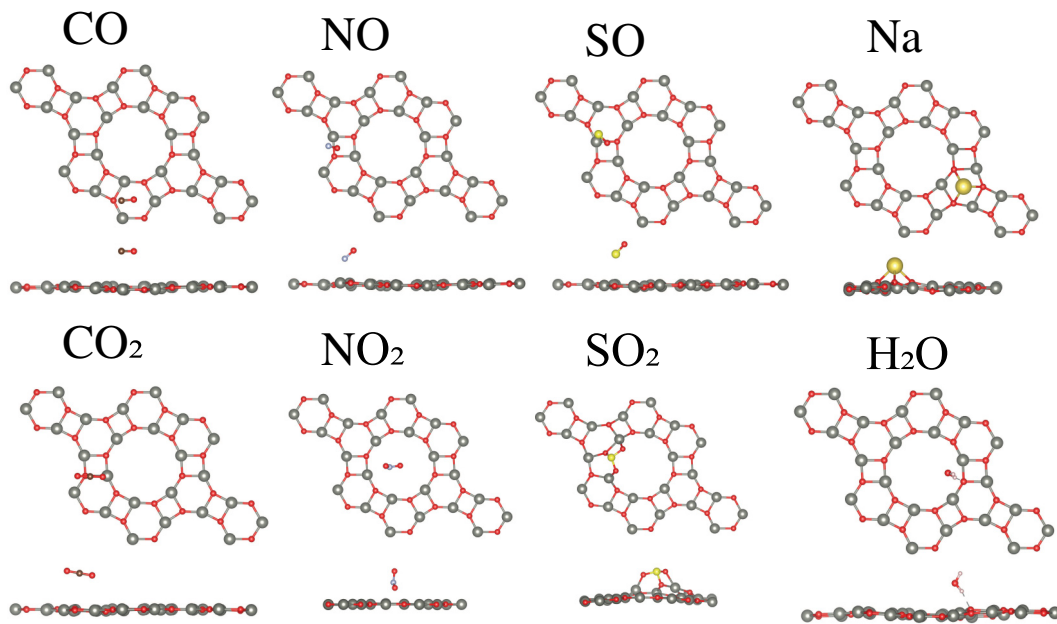
FIG. 10.   The optimized structures of *d*-ZnO with adsorbed atom and molecules.

on the ZnO surface, magnetism is induced in the systems. The contribution to the magnetic moment is mainly from the adsorbed molecules. This suggests that there is an orbital reorientation of the localized unpaired electrons, which couple in the parallel spin state with the spins of surrounding electrons, occurs upon the adsorption of these

molecules. An integer magnetic moment per unit cell is found for these NO@ZnO (1 μ_B), SO@ZnO (2 μ_B), and NO$_2$@ZnO (1 μ_B) systems. This shows that these systems would prefer a half-metallic electronic character. Accordingly, the semiconducting property of the bare *d*-ZnO sheet is modulated into half-metallic for NO@ZnO, SO@ZnO,
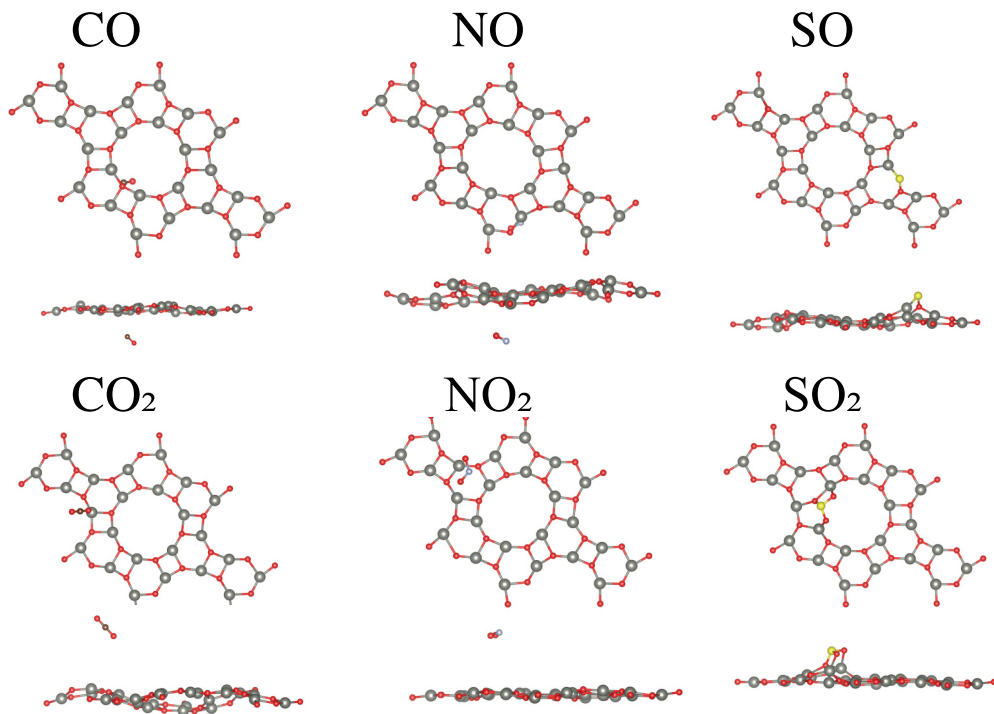

FIG. 11.   The optimized structures of *d*-ZnO with adsorbed atom and molecules at 300 K or a total duration of 2 ps.

and NO_2@ZnO systems. The remaining CO, CO_2, SO_2 cases have their band gap preserved as compared with that of the bare d-ZnO sheet (see Appendix).

It should also be noted that the sensing property of a material is the measure of the material's response to electrical conductivity [111] estimated as $\sigma \propto \exp(-E_g/2k_BT)$. Here E_g stands for the band gap. Based on this expression, an increase or decrease in E_g causes an exponential change in the σ. This means that the molecules would favorably be detected with high sensitivity for the NO@ZnO, SO@ZnO, and NO2@ZnO cases, where the electronic properties of the system change into metal and half-metallic. In addition to the sensing property, the recovery time, τ (desorption rate) of these adsorbed molecules can be roughly estimated as $\tau \propto v \exp(-E_{ads}/k_BT)$. Here, v is the frequency. According to the expression, at approximately 1-THz frequency, the systems (ZnO with adsorbed molecules) with larger positive E_{ads} values would have a longer recovery time (likely to be desorbed and split into subunits), e.g., the SO_2@ZnO system. Those with less positive E_{ads} values would display a shorter recovery time, e.g., NO@ZnO and NO_2@ZnO systems. It is hoped that future experimental studies of the gas-sensing property using the d-ZnO monolayer will confirm our theoretical predictions, because gas adsorption modulates the electronic character of the majority of the systems, resulting in a sensitive variation in the electrical conductance of these systems.

IV. CONCLUSIONS

Based on combined DFT and MD calculations, we report an alternative dodecagonal porous ZnO sheet with potentials for water purification and toxic gas-detection applications. DFT calculations confirm that the d-ZnO sheet exhibits excellent energetic, mechanical, dynamic, and thermal stability. We find that the d-ZnO sheet prefers a nonmagnetic ground state with semiconducting electronic properties. The obtained PBE band gap (2.38 eV) of the ZnO sheet is compared with the PBE+U and HSE06 methods. The results show that Hubbard-U corrections affect the orbital hybridization in the d-ZnO sheet, which in turn enhances the band gap (3.26 eV). The HSE06 obtained band-gap value (4.36 eV) is well above the PBE+U (3.26 eV) results. Moreover, we investigate the potential of the d-ZnO sheet for water desalination. Based on the CI NEB calculations, the deduced $E_{barrier}$ for H_2O molecule is 0.29 eV while those for Na^+ ion and Cl^- ion are 1.81 and 0.77 eV, respectively. The $E_{barrier}$ value for Na^+ ion and Cl^- ion are sufficiently high enough to trap the Na^+ ion and Cl^- ion, while that of H_2O is the lowest. This means that H_2O passing through the d-ZnO pore will experience only minor repulsion. In addition to the DFT calculations, the molecular dynamics simulations provide useful insights on the interaction of water with a d-ZnO sheet. It is found

that the proposed membrane d-ZnO sheet demonstrates a very good water flux and grows with increasing pressure and temperature. For further investigations, the adsorption properties of some selected toxic gases (CO, SO, NO, CO_2, SO_2, and NO_2) on d-ZnO systems have been investigated. At 0 K, the calculated chemisorption energies show that NO_2 and SO_2 would preferentially be detected on the d-ZnO substrate as compared to CO, NO, SO, and CO_2 molecules when these gases are simultaneously released at the constant pressure on the d-ZnO surface. It is revealed that at 300 K, the d-ZnO surface appears to be unsuitable for CO, CO_2, NO, and NO_2 gas sensors. More interestingly, the SO molecule, which is weakly physisorbed at 0 K, decomposes into S and O at 300 K. An integer magnetic moment per unit cell is found for these NO@ZnO (1 μ_B), SO@ZnO (2 μ_B) and NO_2@ZnO (1 μ_B) systems. Accordingly, the semiconducting property of the bare ZnO sheet is modulated into half-metallic for NO@ZnO, SO@ZnO, and NO_2@ZnO systems. Our results suggest a promising route to design the porous d-ZnO sheet for water desalination and toxic detection applications.
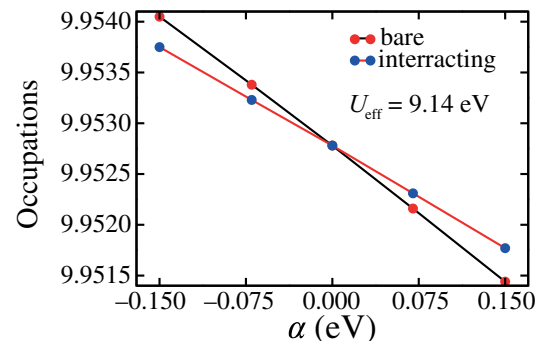
FIG. 12. Linear response of d orbital occupations as a function of potential shift α. The curves depicted by the red and blue circles lines are labeled bare and interacting. The inverse response functions are deduced numerically by calculating the slope of the curves. x_0 follows from the slope of curve bare, whereas x from the slope of curve interacting.
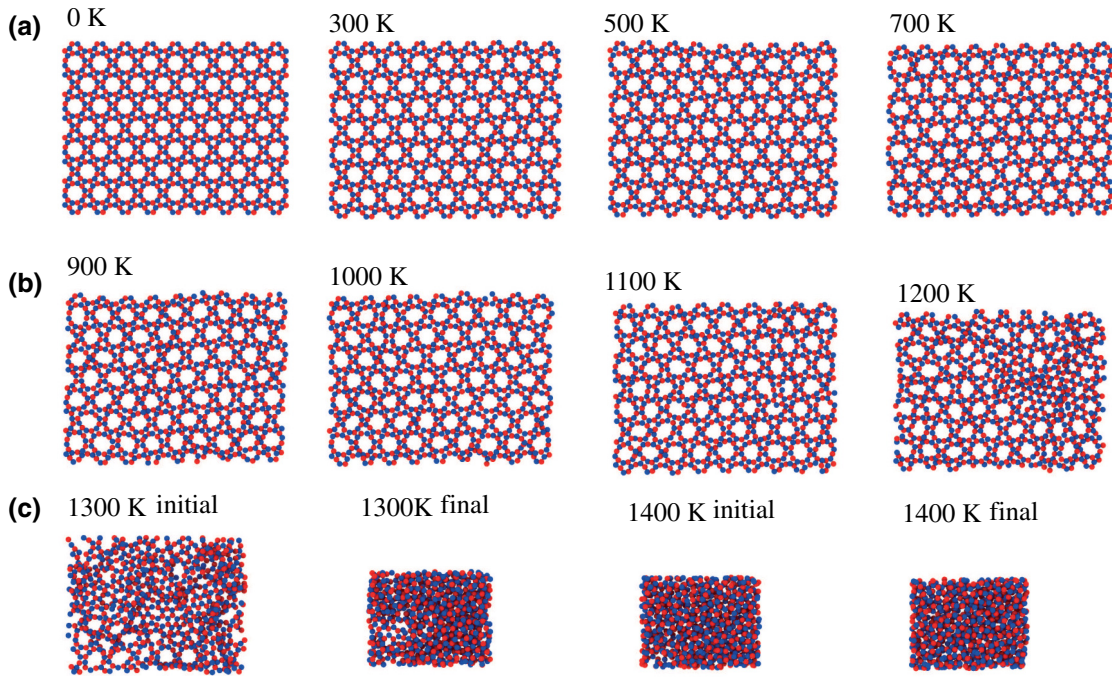
FIG. 13.   The snapshots of the atomic configurations of the *d*-ZnO structure taken from MD simulations performed from at 0 to 1400 K.

APPENDIX

In this Appendix we present Hubbard U calculation results, snapshots of the first frame of heating simulations of *d*-ZnO nanosheets. Top views of the *d*-ZnO structure from 0 to 1400 K are also given. In addition, the adsorption sites for molecules on the *d*-ZnO, the optimized structures of *d*-ZnO with adsorbed adatom and molecules, the optimized structures of *d*-ZnO with adsorbed atom and molecules at 300 K and corresponding density of states (DOS) of *d*-ZnO with adsorbed atom and molecules are given in this Appendix

To evaluate the U parameter to use in this study we use the linear response approach formulated by Cococcioni *et al.* [69], as implemented in the Quantum ESPRESSO package [76]. In the linear-response scheme calculations, we first compute x_0 and x, which represent the noninteracting (bare) and interacting density response functions of the
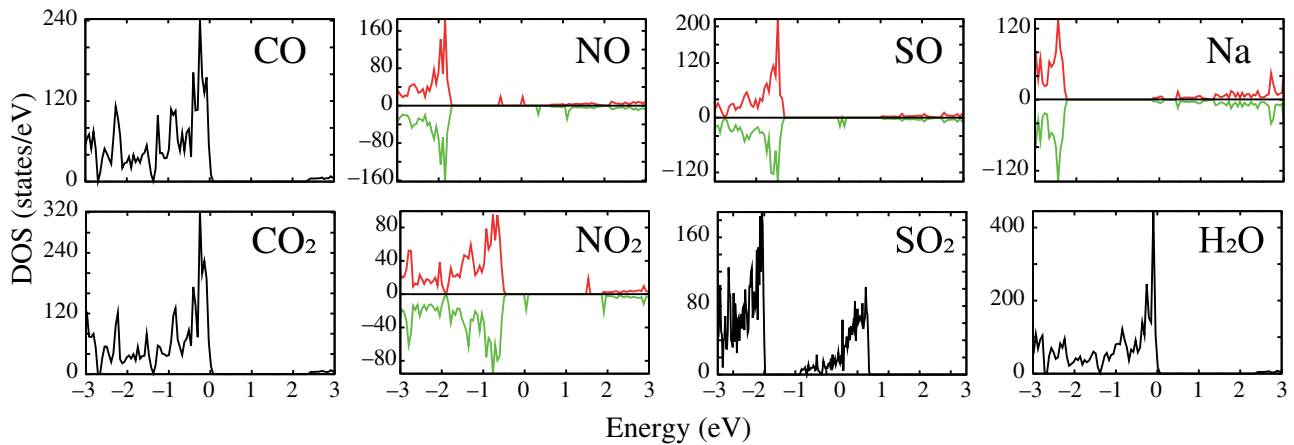

FIG. 14.   Density of states (DOS) of *d*-ZnO with adsorbed atom and molecules.

system with respect to localized perturbations, as displayed in Fig. 12. The parameter U_{eff} is then obtained from the expression $U_{\text{eff}} = (x_0^{-1} - x^{-1})$. The calculated U_{eff} value for d-ZnO is 9.14 eV.

The d-ZnO nanosheets sustain its dodecagonal structure up to 1000 K (see Fig. 13). Our MD simulations show that some of the Zn-O bonds start to dissociate at 1100 K. Increasing the temperature results in a phase transition in the d-ZnO sheet and some part of the dodecagonal structure is broken up and turned to hexagonal ZnO structure (at the 1200 K). We continue to increase the temperature and we see that with increasing temperature up to 1300 K, the number of broken bonds between Zn and O are increased. These broken bonds cause formation of bonds between Zn and O atoms, and with increasing the simulation time the 2D d-ZnO structure transferred to the amorf 3D structure. However, we should note that increasing the simulation time and the temperature results in an alternative phase transition for these amorf 3D ZnO and looks like the ZnO starts to crystalize in the wurtzite structure in the hexagonal $P6_3mc$ space group (see Fig. 14).

The total density of states of the Na-adsorbed or molecule-adsorbed d-ZnO monolayer are illustrated in Fig. 14.

---

[1] Y. Gong, L. Shen, Z. Kang, K. Liu, Q. Du, D. Ye, H. Zhao, X. Sun, and J. Zhang, Progress in energy-related graphyne-based materials: Advanced synthesis, functional mechanisms and applications, J. Mater. Chem. A **8**, 21408 (2020).

[2] N. Rono, J. K. Kibet, B. S. Martincigh, and V. O. Nyamori, A review of the current status of graphitic carbon nitride, Crit. Rev. Solid State Mater. Sci. **46**, 189 (2021).

[3] B. Mortazavi, M. Shahrokhi, A. Shapeev, T. Rabczuk, and X. Zhuang, Prediction of C_7N_6 and C_9N_4: Stable and strong porous carbon-nitride nanosheets with attractive electronic and optical properties, J. Mater. Chem. C **7**, 10908 (2019).

[4] S. S. Sani, H. Mousavi, M. Asshabi, and S. Jalilvand, Electronic properties of graphyne and graphdiyne in tight-binding model, ECS J. Solid. State. Sci. Technol. **9**, 031003 (2020).

[5] A. Guirguis, J. W. Maina, X. Zhang, and L. C. Henderson, Applications of nano-porous graphene materials–critical review on performance and challenges, Mater. Horiz. **7**, 1218 (2020).

[6] J. Park, P. Bazylewski, and G. Fanchini, Porous graphene-based membranes for water purification from metal ions at low differential pressures, Nanoscale **8**, 9563 (2016).

[7] T. A. Tabish, F. A. Memon, D. E. Gomez, D. W. Horsell, and S. Zhang, A facile synthesis of porous graphene for efficient water and wastewater treatment, Sci. Rep. **8**, 1 (2018).

[8] T. Wu, F. Moghadam, and K. Li, High-performance porous graphene oxide hollow fiber membranes with tailored pore sizes for water purification, J. Memb. Sci. **645**, 120216 (2022).

[9] D. Cohen-Tanugi and J. Grossman, Water desalination across nanoporous graphene, Nano Lett. **12**, 3602 (2012).

[10] J. Lim and G. Kim, First-principles modeling of water permeation through periodically porous graphene derivatives, J. Colloid Interface Sci. **538**, 367 (2019).

[11] S. P. Surwade, S. N. Smirnov, I. V. Vlassiouk, R. R. Unocic, G. M. Veith, S. Dai, and S. M. Mahurin, Water desalination using nanoporous single-layer graphene, Nat. Nanotechnol. **10**, 459 (2015).

[12] S. Remanan, N. Padmavathy, S. Ghosh, S. Mondal, S. Bose, and N. C. Das, Porous graphene-based membranes: preparation and properties of a unique two-dimensional nanomaterial membrane for water purification, Sep. Purif. Rev. **50**, 262 (2021).

[13] H. Qiu, M. Xue, C. Shen, Z. Zhang, and W. Guo, Graphynes for water desalination and gas separation, Adv. Mater. **31**, 1803772 (2019).

[14] T. Ashirov and A. Coskun, Ultrahigh permeance metal coated porous graphene membranes with tunable gas selectivities, Chem **7**, 2385 (2021).

[15] C. Chakravarty, B. Mandal, and P. Sarkar, Porous graphene–fullerene nanocomposites: A new composite for solar cell and optoelectronic applications, J. Phys. Chem. C **122**, 15835 (2018).

[16] H. Yoon, J. Nah, H. Kim, S. Ko, M. Sharifuzzaman, S. C. Barman, X. Xuan, J. Kim, and J. Y. Park, A chemically modified laser-induced porous graphene based flexible and ultrasensitive electrochemical biosensor for sweat glucose detection, Sens. Actuators, B **311**, 127866 (2020).

[17] J. Buchheim, K.-P. Schlichting, R. M. Wyss, and H. G. Park, Assessing the thickness–permeation paradigm in nanoporous membranes, ACS Nano **13**, 134 (2018).

[18] J. C. Jia, L. Yang, Y. Zhang, X. Zhang, K. Xiao, J. Xu, and J. Liu, Graphitic carbon nitride films: Emerging paradigm for versatile applications, ACS Appl. Mater. Interfaces **12**, 53571 (2020).

[19] X. Huo, H. Yi, Y. Fu, Z. An, L. Qin, X. Liu, B. Li, S. Liu, L. Li, and M. Zhang, *et al.*, Porous graphitic carbon nitride nanomaterials for water treatment, Environ. Sci. Nano **8**, 1835 (2021).

[20] J. Tan, Z. Li, J. Li, J. Wu, X. Yao, and T. Zhang, Graphitic carbon nitride-based materials in activating persulfate for aqueous organic pollutants degradation: A review on materials design and mechanisms, Chemosphere **262**, 127675 (2021).

[21] A. Akhundi, A. Badiei, G. M. Ziarani, A. Habibi-Yangjeh, M. J. Munoz-Batista, and R. Luque, Graphitic carbon nitride-based photocatalysts: Toward efficient organic transformation for value-added chemicals production, Mol. Catal. **488**, 110902 (2020).

[22] S. Wang, J. Zhang, B. Li, H. Sun, and S. Wang, Engineered graphitic carbon nitride-based photocatalysts for visible-light-driven water splitting: A review, Energy Fuels **35**, 6504 (2021).

[23] H. Basharnavaz, A. Habibi-Yangjeh, and M. Pirhashemi, Graphitic carbon nitride as a fascinating adsorbent for toxic gases: A mini-review, Chem. Phys. Lett. **754**, 137676 (2020).

[24] B. Jürgens, E. Irran, J. Senker, P. Kroll, H. Müller, and W. Schnick, Melem (2, 5, 8-triamino-tri-s-triazine), an important intermediate during condensation of melamine rings to graphitic carbon nitride: Synthesis, structure determination by x-ray powder diffractometry, solid-state NMR, and theoretical studies, J. Am. Chem. Soc. **125,** 10288 (2003).

[25] M. Sun, X. Wei, J. Zhang, Y. Huang, and G. Zhu, First-principles study on the type-II *g*-C_6N_6/GaS heterojunction: A promising photocatalyst for water splitting, Diam. Relat. Mater. **110,** 108157 (2020).

[26] Z. Ma, X. Zhao, Q. Tang, and Z. Zhou, Computational prediction of experimentally possible *g*-C_3N_3 monolayer as hydrogen purification membrane, Int. J. Hydrogen Energy **39,** 5037 (2014).

[27] F. Li, Y. Qu, and M. Zhao, Efficient helium separation of graphitic carbon nitride membrane, Carbon **95,** 51 (2015).

[28] S. W. De Silva, A. Du, W. Senadeera, and Y. Gu, Strained graphitic carbon nitride for hydrogen purification, J. Memb. Sci. **528,** 201 (2017).

[29] Y. Ji, H. Dong, H. Lin, L. Zhang, T. Hou, and Y. Li, Heptazine-based graphitic carbon nitride as an effective hydrogen purification membrane, RSC Adv. **6,** 52377 (2016).

[30] Y. Cui, X. An, S. Zhang, Q. Tang, H. Lan, H. Liu, and J. Qu, Emerging graphitic carbon nitride-based membranes for water purification, Water Res. **200,** 117207 (2021).

[31] J. Tan, N. Tian, Z. Li, J. Li, X. Yao, M. Vakili, Y. Lu, and T. Zhang, Intrinsic defect engineering in graphitic carbon nitride for photocatalytic environmental purification: A review to fill existing knowledge gaps, Chem. Eng. J. **421,** 127729 (2021).

[32] Y. Z. Abdullahi, T. L. Yoon, and A. A. Kassimu, Metal-free ferromagnetic semiconductor: Mechanical, electronic and magnetic properties of boron doped graphitic carbon nitride (*g*-C_6N_6) sheet, Mater. Chem. Phys. **254,** 123470 (2020).

[33] Z. Chen, J. Zhao, C. R. Cabrera, and Z. Chen, Computational screening of efficient single-atom catalysts based on graphitic carbon nitride (*g*-C_3N_4) for nitrogen electroreduction, Small Methods **3,** 1800368 (2019).

[34] A. Habibi-Yangjeh and H. Basharnavaz, Remarkable improvement in hydrogen storage capabilities of graphitic carbon nitride nanosheets under selected transition metal embedding: A DFT study, Int. J. Hydrogen Energy **46,** 33864 (2021).

[35] Z. Zhao, W. Zhang, W. Liu, Y. Li, J. Ye, J. Liang, and M. Tong, Activation of sulfite by single-atom Fe deposited graphitic carbon nitride for diclofenac removal: The synergetic effect of transition metal and photocatalysis, Chem. Eng. J. **407,** 127167 (2021).

[36] Y. Shimoyama, K. Koga, H. Tabe, Y. Yamada, Y. Kon, and D. Hong, RuO_2 nanoparticle-embedded graphitic carbon nitride for efficient photocatalytic H_2 evolution, ACS Appl. Nano Mater. **4,** 11700 (2021).

[37] X.-W. Guo, S.-M. Chen, H.-J. Wang, Z.-M. Zhang, H. Lin, L. Song, and T.-B. Lu, Single-atom molybdenum immobilized on photoactive carbon nitride as efficient photocatalysts for ambient nitrogen fixation in pure water, J. Mater. Chem. A **7,** 19831 (2019).

[38] Y. Z. Abdullahi, T. L. Yoon, M. M. Halim, M. R. Hashim, and T. L. Lim, Effects of atoms and molecules adsorption on electronic and magnetic properties of s-triazine with embedded Fe atom: DFT investigations, Philos. Mag. **98,** 1114 (2018).

[39] Y. Z. Abdullahi, T. L. Yoon, and T. L. Lim, Adsorption and decomposition of H_2S on C_2N sheet with embedded manganese atom: First-principles calculations, Chem. Phys. **555,** 111443 (2021).

[40] M. Mushtaq, S. Khan, and N. Tit, Magnetization effect of Mn-embedded in C_2N on hydrogen adsorption and gas-sensing properties: Ab-initio analysis, Appl. Surf. Sci. **537,** 147970 (2021).

[41] M. Mushtaq and N. Tit, Magnetic single atom catalyst in C_2N to induce adsorption selectivity toward oxidizing gases, Sci. Rep. **11,** 1 (2021).

[42] I. Cabria, M. López, and J. Alonso, Theoretical study of the transition from planar to three-dimensional structures of palladium clusters supported on graphene, Phys. Rev. B **81,** 035403 (2010).

[43] E. Fırıncı, Pyrimidine-2, 4, 6-trione copper(II) complexes and their catalytic activities in the peroxidative oxidation of cyclohexane, J. Mol. Struct. **1193,** 125 (2019).

[44] E. Fırıncı, Copper (II) complexes with barbiturate derivatives: Synthesis, characterization and catalytic applications, Polyhedron **164,** 132 (2019).

[45] W. Li, Y. Yang, J. K. Weber, G. Zhang, and R. Zhou, Tunable, strain-controlled nanoporous MoS_2 filter for water desalination, ACS Nano **10,** 1829 (2016).

[46] M. Heiranian, A. B. Farimani, and N. R. Aluru, Water desalination with a single-layer MoS_2 nanopore, Nat Commun. **6,** 8616 (2015).

[47] Y. Şahin, S. Öztürk, N. Kılınc, A. Kösemen, M. Erkovan, and Z. Z. Öztürk, Electrical conduction and NO2 gas sensing properties of ZnO nanorods, Appl. Surf. Sci. **303,** 90 (2014).

[48] E. R. Waclawik, J. Chang, A. Ponzoni, I. Concina, D. Zappa, E. Comini, N. Motta, G. Faglia, and G. Sberveglieri, Functionalised zinc oxide nanowire gas sensors: Enhanced NO2 gas sensor response by chemical modification of nanowire surfaces, Beilstein J. Nanotechnol. **3,** 368 (2012).

[49] S. Abubakar, J. L. Y. Chyi, S. T. Tan, S. Sagadevan, Z. A. Talib, and S. Paiman, Nanoscale domain imaging and the electromechanical response of zinc oxide nanorod arrays synthesized on different substrates, J. Mater. Res. Technol. **14,** 2451 (2021).

[50] H.-U. Lee, K. Ahn, S.-J. Lee, J.-P. Kim, H.-G. Kim, S.-Y. Jeong, and C.-R. Cho, ZnO nanobarbed fibers: Fabrication, sensing NO2 gas, and their sensing mechanism, Appl. Phys. Lett. **98,** 193114 (2011).

[51] S.-W. Fan, A. K. Srivastava, and V. P. Dravid, Nanopatterned polycrystalline ZnO for room temperature gas sensing, Sens. Actuators, B **144,** 159 (2010).

[52] J. Wang, X. Sun, Y. Yang, and C.M.L. Wu, N–P transition sensing behaviors of ZnO nanotubes exposed to NO_2 gas, Nanotechnology **20,** 465501 (2009).

[53] P. Rai, S. Raj, K.-J. Ko, K.-K. Park, and Y.-T. Yu, Synthesis of flower-like ZnO microstructures for gas sensor applications, Sens. Actuators, B **178,** 107 (2013).

[54] A. Forleo, L. Francioso, S. Capone, P. Siciliano, P. Lommens, and Z. Hens, Synthesis and gas sensing properties of ZnO quantum dots, Sens. Actuators, B **146,** 111 (2010).

[55] P. Rai and Y.-T. Yu, Citrate-assisted hydrothermal synthesis of single crystalline ZnO nanoparticles for gas sensor application, Sens. Actuators, B **173,** 58 (2012).

[56] J. Zhang, S. Wang, Y. Wang, M. Xu, H. Xia, S. Zhang, W. Huang, X. Guo, and S. Wu, ZnO hollow spheres: Preparation, characterization, and gas sensing properties, Sens. Actuators, B **139,** 411 (2009).

[57] M. Z. Ahmad, J. Chang, M. S. Ahmad, E. R. Waclawik, and W. Wlodarski, Non-aqueous synthesis of hexagonal ZnO nanopyramids: gas sensing properties, Sens. Actuators, B **177,** 286 (2013).

[58] D. Calestani, M. Zha, R. Mosca, A. Zappettini, M. Carotta, V. Di Natale, and L. Zanotti, Growth of ZnO tetrapods for nanostructure-based gas sensors, Sens. Actuators, B **144,** 472 (2010).

[59] F. Liu, X. Wang, X. Chen, X. Song, J. Tian, and H. Cui, Porous ZnO ultrathin nanosheets with high specific surface areas and abundant oxygen vacancies for acetylacetone gas sensing, ACS. Appl. Mater. Interfaces **11,** 24757 (2019).

[60] H. Suzuki, I. Miyazato, T. Hussain, F. Ersan, S. Maeda, and K. Takahashi, Designing two-dimensional dodecagonal boron nitride, CrystEngComm **24,** 471 (2022).

[61] Q. Li, D. Chen, J. Miao, S. Lin, Z. Yu, D. Cui, Z. Yang, and X. Chen, Highly sensitive sensor based on ordered porous ZnO nanosheets for ethanol detecting application, Sens. Actuators, B **326,** 128952 (2021).

[62] M. S. Choi, M. Y. Kim, A. Mirzaei, H.-S. Kim, S.-i. Kim, S.-H. Baek, D. W. Chun, C. Jin, and K. H. Lee, Selective, sensitive, and stable NO2 gas sensor based on porous ZnO nanosheets, Appl. Surf. Sci. **568,** 150910 (2021).

[63] L. Zhang, B. Chen, L. Xie, and Z. Li, Study on the antimicrobial properties of ZnO suspension against Gram-positive and Gram-negative bacteria strains, Adv. Mat. Res. **393,** 1488 (2012).

[64] P. Stoimenov, R. Klinger, G. Marchin, and K. Klabunde, Metal oxide nanoparticles as bactericidal agents, Langmuir **18,** 6679 (2002).

[65] N. Padmavathy and R. Vijayaraghavan, Enhanced bioactivity of ZnO nanoparticles—an antimicrobial study, Sci. Technol. Adv. Mater. **9,** 035004 (2008).

[66] G. Kresse and J. Furthmüller, Efficient iterative schemes for ab initio total-energy calculations using a plane-wave basis set, Phys. Rev. B **54,** 11169 (1996).

[67] P. Hohenberg and W. Kohn, Inhomogeneous electron gas, Phys. Rev. **136,** B864 (1964).

[68] J. Perdew, K. Burke, and M. Ernzerhof, Generalized Gradient Approximation Made Simple, Phys. Rev. Lett. **77,** 3865 (1996).

[69] M. Cococcioni and S. De Gironcoli, Linear response approach to the calculation of the effective interaction parameters in the LDA+U method, Phys. Rev. B **71,** 035105 (2005).

[70] Y. Z. Abdullahi, Z. Vatansever, E. Aktürk, Ü. Akıncı, and O. Aktürk, Doping-driven antiferromagnetic to ferromagnetic phase transition in tetragonal Cr$_2$B$_2$ monolayer, Phys. Status Solidi (b) **258,** 2000396 (2021).

[71] Y. Z. Abdullahi, Z. Vatansever, E. Aktürk, Ü. Akıncı, and O. Aktürk, A tetragonal phase Mn$_2$B$_2$ sheet: A stable room temperature ferromagnet with sizable magnetic anisotropy, Phys. Chem. Chem. Phys. **22,** 10893 (2020).

[72] S. Grimme, Semiempirical GGA-type density functional constructed with a long-range dispersion correction, J. Comput. Chem. **27,** 1787 (2006).

[73] H. Monkhorst and J. Pack, Special points for Brillouin-zone integrations, Phys. Rev. B **13,** 5188 (1976).

[74] X. Gonze and C. Lee, Dynamical matrices, Born effective charges, dielectric permittivity tensors, and interatomic force constants from density-functional perturbation theory, Phys. Rev. B **55,** 10355 (1997).

[75] G. Henkelman, B. Uberuaga, and H. Jónsson, A climbing image nudged elastic band method for finding saddle points and minimum energy paths, J. Chem. Phys. **113,** 9901 (2000).

[76] P. Giannozzi, S. Baroni, N. Bonini, M. Calandra, R. Car, C. Cavazzoni, D. Ceresoli, G. Chiarotti, M. Cococcioni, and I. Dabo, *et al.*, QUANTUM ESPRESSO: a modular and open-source software project for quantum simulations of materials, J. Phys.: Condens. Matter **21,** 395502 (2009).

[77] A. Thompson, H. Aktulga, R. Berger, D. Bolintineanu, W. Brown, P. Crozier, P. Veld, A. Kohlmeyer, S. Moore, T. Nguyen, R. Shan, W. Stevens, J. Tranchida, C. Trott, and S. Plimpton, LAMMPS—a flexible simulation tool for particle-based materials modeling at the atomic, meso, and continuum scales, Comput. Phys. Commun. **271,** 108171 (2022).

[78] A. Duin, S. Dasgupta, F. Lorant, and W. Goddard, ReaxFF: A reactive force field for hydrocarbons, J. Phys. Chem. A **105,** 9396 (2001).

[79] D. Raymand, A. Van Duin, D. Spångberg, W. Goddard, and K. Hermansson, Water adsorption on stepped ZnO surfaces from MD simulation, Surf. Sci. **604,** 741 (2010).

[80] M. Fedkin, Y. Shin, N. Dasgupta, J. Yeon, W. Zhang, D. Van Duin, A. Van Duin, K. Mori, A. Fujiwara, and M. Machida, *et al.*, Development of the ReaxFF methodology for electrolyte–water systems, J. Phys. Chem. A **123,** 2125 (2019).

[81] A. Stukowski, Visualization and analysis of atomistic simulation data with OVITO–the Open Visualization Tool, Modell. Simul. Mater. Sci. Eng. **18,** 015012 (2009).

[82] W. Humphrey, A. Dalke, and K. Schulten, VMD: Visual molecular dynamics, J. Mol. Graph. **14,** 33 (1996).

[83] R. Bader, Atoms in molecules, Acc. Chem. Res. **18,** 9 (1985).

[84] L. Hu, X. Wu, and J. Yang, Mn$_2$C monolayer: A 2D anti-ferromagnetic metal with high Néel temperature and large spin–orbit coupling, Nanoscale **8,** 12939 (2016).

[85] S. Cahangirov, M. Topsakal, E. Aktürk, H. Şahin, and S. Ciraci, Two- and One-dimensional Honeycomb Structures of Silicon and Germanium, Phys. Rev. Lett. **102,** 236804 (2009).

[86] M. Topsakal, S. Cahangirov, and S. Ciraci, The response of mechanical and electronic properties of graphane to the elastic strain, Appl. Phys. Lett. **96,** 091912 (2010).

[87] H. Şahin, S. Cahangirov, M. Topsakal, E. Bekaroglu, E. Akturk, R. Senger, and S. Ciraci, Monolayer honeycomb

structures of group-IV elements and III-V binary compounds: First-principles calculations, Phys. Rev. B **80,** 155453 (2009).

[88] F. Mouhat and F. Coudert, Necessary and sufficient elastic stability conditions in various crystal systems, Phys. Rev. B **90,** 224104 (2014).

[89] H. Yu, M. Liao, W. Zhao, G. Liu, X. Zhou, Z. Wei, X. Xu, K. Liu, Z. Hu, and K. Deng, *et al.*, Wafer-scale growth and transfer of highly-oriented monolayer MoS$_2$ continuous films, ACS Nano. **11,** 12001 (2017).

[90] Z. Zhang, Y. Gong, X. Zou, P. Liu, P. Yang, J. Shi, L. Zhao, Q. Zhang, L. Gu, and Y. Zhang, Epitaxial growth of two-dimensional metal–semiconductor transition-metal dichalcogenide vertical stacks (VSe$_2$/MX$_2$) and their band alignments, ACS Nano **13,** 885 (2018).

[91] F. Li, Y. Feng, Z. Li, C. Ma, J. Qu, X. Wu, D. Li, X. Zhang, T. Yang, and Y. He, *et al.*, Rational kinetics control toward universal growth of 2D vertically stacked heterostructures, Adv. Mater. **31,** 1901351 (2019).

[92] J. Mahmood, E. Lee, M. Jung, D. Shin, I. Jeon, S. Jung, H. Choi, J. Seo, S. Bae, and S. Sohn, *et al.*, Nitrogenated holey two-dimensional structures, Nat. Commun. **6,** 1 (2015).

[93] I. Lucci, S. Charbonnier, L. Pedesseau, M. Vallet, L. Cerutti, J. Rodriguez, E. Tournié, R. Bernard, A. Létoublon, and N. Bertru, *et al.*, Universal description of III-V/Si epitaxial growth processes, Phys. Rev. Mater. **2,** 060401 (2018).

[94] D. Pan, D. Fan, N. Kang, J. Zhi, X. Yu, H. Xu, and &J. Zhao, Free-standing two-dimensional single-crystalline InSb nanosheets, Nano Lett. **16,** 834 (2016).

[95] H. Henck, J. Avila, Z. Aziza, D. Pierucci, J. Baima, B. Pamuk, J. Chaste, D. Utt, M. Bartos, and K. Nogajewski, *et al.*, Flat electronic bands in long sequences of rhombohedral-stacked graphene, Phys. Rev. B **97,** 245421 (2018).

[96] A. Kuklin, S. Shostak, and A. Kuzubov, Two-dimensional lattices of VN: Emergence of ferromagnetism and half-metallicity on nanoscale, J. Phys. Chem. Lett. **9,** 1422 (2018).

[97] T. Bilitewski and R. Moessner, Disordered flat bands on the kagome lattice, Phys. Rev. B **98,** 235109 (2018).

[98] S. Park, S. Kang, H. Kim, K. Lee, P. Kim, S. Sim, N. Lee, B. Karuppannan, and J. Kim, *et al.*, Kagome van-der-Waals Pd$_3$P$_2$S$_8$ with flat band, Sci. Rep. **10,** 1 (2020).

[99] D. Bergman, C. Wu, and L. Balents, Band touching from real-space topology in frustrated hopping models, Phys. Rev. B **78,** 125104 (2008).

[100] J. You, B. Gu, and G. Su, Flat band and hole-induced ferromagnetism in a novel carbon monolayer, Sci. Rep. **9,** 1 (2019).

[101] Y. Z. Abdullahi, Z. Vatansever, F. Ersan, U. Akinci, O. Akturk, and E. Akturk, Ferromagnetic TM$_2$BC (TM = Cr, Mn) monolayers for spintronic devices with high Curie temperature, Phys. Chem. Chem. Phys. **23,** 6107 (2021).

[102] M. Han, H. Inoue, S. Fang, C. John, L. Ye, M. Chan, D. Graf, T. Suzuki, M. Ghimire, and W. Cho, *et al.*, Evidence of two-dimensional flat band at the surface of antiferromagnetic kagome metal FeSn, Nat. Commun. **12,** 1 (2021).

[103] Y. Z. Abdullahi, F. Ersan, Z. Vatansever, E. Aktürk, and O. Aktürk, Exploring the potential of MnX (S, Sb) monolayers for antiferromagnetic spintronics: A theoretical investigation, J. Appl. Phys. **128,** 113903 (2020).

[104] R. Babicheva, S. Dmitriev, A. Kistanov, M. Dahanayaka, A. Law, and K. Zhou, New carbon membrane for water desalination via reverse osmosis, IOP Conf. Ser.: Mater. Sci. Eng. **447,** 012053 (2018).

[105] B. Liu, A. Law, and K. Zhou, Strained single-layer C2N membrane for efficient seawater desalination via forward osmosis: A molecular dynamics study, J. Memb. Sci. **550,** 554 (2018).

[106] F. Ersan, H. Ozaydin, G. Gökoğlu, and E. Aktürk, Theoretical investigation of lithium adsorption, diffusion and coverage on MX$_2$ (M = Mo, W; X = O, S, Se, Te) monolayers, Appl. Surf. Sci. **425,** 301 (2017).

[107] T. Yang, B. Zheng, Z. Wang, T. Xu, C. Pan, J. Zou, X. Zhang, Z. Qi, H. Liu, and Y. Feng, *et al.*, Van der Waals epitaxial growth and optoelectronics of large-scale WSe$_2$/SnS$_2$ vertical bilayer *p*-*n* junctions, Nat. Commun. **8,** 1 (2017).

[108] K. Yin, S. Huang, X. Chen, X. Wang, J. Kong, Y. Chen, and J. Xue, Generating sub-nanometer pores in single-layer MoS$_2$ by heavy-ion bombardment for gas separation: A theoretical perspective, ACS Appl. Mater. Interfaces **10,** 28909 (2018).

[109] B. Huang, Z. Li, Z. Liu, G. Zhou, S. Hao, J. Wu, B. Gu, and W. Duan, Adsorption of gas molecules on graphene nanoribbons and its implication for nanoscale molecule sensor, J. Phys. Chem. C **112,** 13442 (2008).

[110] G. Martyna, M. Klein, and M. Tuckerman. Nosé–Hoover chains, The canonical ensemble via continuous dynamics, J. Chem. Phys. **97,** 2635 (1992).

[111] F. Schedin, A. Geim, S. Morozov, E. Hill, P. Blake, M. Katsnelson, and K. Novoselov, Detection of individual gas molecules adsorbed on graphene, Nat. Mater. **6,** 652 (2007).